Journal of Catalysis 395 (2021) 315–324

Contents lists available at ScienceDirect

Journal of Catalysis

journal homepage: www.elsevier.com/locate/jcat

Near ambient-pressure X-ray photoelectron spectroscopy study of CO_2 activation and hydrogenation on indium/copper surface

Mo Li [a,b], Wen Luo [a,b,c,*], Andreas Züttel [a,b]

[a] Laboratory of Materials for Renewable Energy (LMER), Institute of Chemical Sciences and Engineering (ISIC), Basic Science Faculty (SB), École Polytechnique Fédérale de Lausanne (EPFL) Valais/Wallis, Energypolis, Rue de l'Industrie 17, CH-1951 Sion, Switzerland
[b] Empa Materials Science and Technology, CH-8600 Dübendorf, Switzerland
[c] School of Environmental and Chemical Engineering, Shanghai University, 99 Shangda Road, Shanghai 200444, China

ARTICLE INFO

Article history:
Received 13 October 2020
Revised 5 January 2021
Accepted 7 January 2021
Available online 1 February 2021

Keywords:
Cu-In bimetallic catalyst
CO_2 hydrogenation
Reaction mechanism
Oxygen vacancy
Near ambient-pressure X-ray photoelectron spectroscopy (NAP-XPS)

ABSTRACT

Indium-based catalysts exhibit excellent performance for CO_2 hydrogenation to methanol, yet their nature and chemical evolution under reaction conditions are still elusive, thus hindering an understanding of their reaction mechanism. In this work, near ambient-pressure X-ray photoelectron spectroscopy (NAP-XPS) is employed to investigate the chemical properties and the catalytic role of indium/copper model catalysts under CO_2 hydrogenation conditions. We found that the deposition of In on the surface of a Cu foil led to the formation of Cu-In alloy, whereas upon CO_2 exposure, In was partially oxidized to In_2O_{3-x} and Cu remains metallic. Due to the presence of In_2O_{3-x}, CO_2 was activated on the surface of In/Cu samples mainly in the form of carbonate. In addition, compared with the pure In foil reference, both the fraction of oxygen vacancies and the coverage density of carbonate were higher on the In/Cu samples, indicating the promotion effect of Cu-In alloy in the activation of CO_2. These results reveal the evolution of the active sites of indium/copper catalysts and inspire the design of advanced In-based bimetallic catalysts for CO_2 hydrogenation.

1. Introduction

In the framework of research devoted to meeting the growing energy demands, the catalytic conversion of CO_2 to value-added chemicals and fuels with the assistance of H_2 has been proven to be a feasible and promising approach, as it both mitigates global warming caused by conventional fossil fuels and provides a solution to the storage of renewable energy [1–3]. Although the process is attractive, its scale-up remains a great challenge due to the lack of efficient and selective catalysts, as well as its unclear reaction mechanism. Thus, understanding the activation and reduction of CO_2 on a catalyst surface is imperative for the development of advanced catalyst and the eventual industrialization of CO_2 hydrogenation.

Recently, In_2O_3 has emerged as a promising material for converting CO_2 to methanol via hydrogenation [4–7]. For example, using pure In_2O_3 as catalyst, the reverse water-gas shift (RWGS) reaction can be completely suppressed, leading to a nearly 100% methanol selectivity (5 MPa, 16,000 h^{-1} GHSV, 200–300 °C). Density functional theory (DFT) calculations have suggested that the presence of oxygen vacancies on the In_2O_3 surface favors the methanol synthesis pathway [8,9]. The existence of oxygen vacancies has also been proven experimentally using electron paramagnetic resonance (EPR), temperature-programmed desorption (CO_2-TPD), and Raman spectroscopy, *etc.* [5,7,10]. Recently, an *operando* X-ray powder diffraction (XRD) - X-ray absorption spectroscopy (XAS) study directly correlated the activation of In_2O_3 catalysts to the formation of oxygen vacancies, and deactivation to the appearance of over reduced metallic In [11]. Nevertheless, surface-sensitive studies are still required to reveal the chemical state of In_2O_3 and adsorbates under reaction conditions.

Although In_2O_3 is highly selective and durable for CO_2 hydrogenation, its low H_2-splitting ability limits its CO_2 conversion rate. Therefore, metals such as Cu [12–15], Pd [16–19], Ni [20], and Au [21] have been integrated with In_2O_3-based catalysts, with the intention to enhance the H_2-splitting ability. However, the formation of alloys between In and other metals (*e.g.*, Cu or Pd) makes it difficult to identify the catalytic sites and the reaction mechanism under the CO_2 reduction environment. For example, Shi et al. suggested that the formation of $Cu_{11}In_9$ improves the dissociation of

* Corresponding author at: Laboratory of Materials for Renewable Energy (LMER), Institute of Chemical Sciences and Engineering (ISIC), Basic Science Faculty (SB), École Polytechnique Fédérale de Lausanne (EPFL) Valais/Wallis, Energypolis, Rue de l'Industrie 17, CH-1951 Sion, Switzerland.
E-mail address: wen.luo@epfl.ch (W. Luo).

https://doi.org/10.1016/j.jcat.2021.01.010
0021-9517/

H_2 to atomic hydrogen, which then participates in CO_2 hydrogenation to methanol [13]. However, Yao et al. proposed that metallic Cu sites adsorb and dissociate H_2 for the hydrogenation of adsorbed CO_2 on the surface of In_2O_3 [15]. Similar arguments also hold for Pd-In_2O_3 catalytic systems. These arguments for the function of the bimetallic phases might originate from the extensively employed *ex situ* characterization techniques on these bimetallic catalysts after exposure to air, which is exclusively undesirable for bimetallic alloy phases and oxygen vacancies due to the potential oxidation. Therefore, it is important to investigate In_2O_3-based bimetallic catalysts (*i.e.*, Cu-In) under CO_2 hydrogenation conditions using *in situ* techniques to understand the structural and compositional evolution of the catalysts.

In this work, the activation of CO_2 on bimetallic In/Cu model catalysts were systematically studied using near ambient-pressure X-ray photoelectron spectroscopy (NAP-XPS). We prepared a series of samples by depositing In on Cu foil, and then probed their surface properties upon exposure to CO_2 and CO_2/H_2 mixtures at different temperatures. We quantified the relative amount of lattice and defect oxygen under different conditions, and observed that the Cu-In alloy corresponded to a higher density of oxygen vacancies, which resulted in a higher coverage density of activated CO_2 in the form of carbonate compared with the pure In reference. Furthermore, we revealed the stability of the oxygen vacancies on In/Cu surfaces at up to 600 K. Based on our experimental observations, we discussed the synergy between the Cu-In alloy phase and the oxygen vacancies from In_2O_{3-x} sites for highly active CO_2 hydrogenation reactions. Overall, our study provides fundamental details of the relationship between the surface property and the performance of Cu-In bimetallic catalysts for CO_2 hydrogenation.

2. Experimental section

In/Cu model catalysts were prepared in the preparation chamber (base pressure 2×10^{-10} mbar) of a laboratory-based NAP-XPS system (SPECS GmbH). A polycrystalline Cu foil (Goodfellow, purity 99.9%, 0.125 mm thick, size 1 cm^2) was cleaned by electrochemical polishing in 85 wt% H_3PO_4 solution at 40 mA for 60 s with another Cu foil as counter electrode before being introduced into the NAP-XPS system. Prior to the In deposition, at least three cycles of Ar^+ sputtering (1.5×10^{-5} mbar Ar, 1 keV, 15 min) and vacuum annealing (850 K, 15 min) were applied to the Cu foil until the level of impurities (O 1s and C 1s) was below the XPS detection limit. In was deposited on the Cu foil from a molybdenum crucible filled with In pellets (Alfa Aesar, purity 99.99%) using an e-beam evaporator (EBE-4, SPECS GmbH) by electron bombardment. The deposition rate was kept constant by maintaining a constant flux current monitored using a built-in flux electrode. A flux current of 10 nA roughly corresponds to a deposition rate of 0.003 ML/s. The morphology of the samples was characterized by a FEI Teneo scanning electron microscope (SEM) operating at a high voltage of 1 kV and a 25 pA beam current, with a working distance of 5–7 mm.

All UHV- and NAP-XPS measurements were carried out in an analysis chamber (base pressure 2×10^{-10} mbar) equipped with a microfocus, monochromatic Al Kα ($h\nu$ = 1486.74 eV) X-ray source, and a differentially pumped hemispherical energy analyzer (PHOIBOS 150 NAP, SPECS GmbH) with a series of electrostatic lenses. For NAP-XPS measurements, the sample is placed in a NAP cell with an X-ray transparent Si_3N_4 window and a 300 μm aperture for the photoelectrons to pass through. With this configuration, XPS measurements can be performed in gas environments up to 25 mbar. Research-grade CO_2 (4.5, PanGas) and H_2 (5.0, PanGas) were used for all experiments and the flowrates were regulated with precise mass flow controllers (GF40, Brooks). The purity of the gases was confirmed with a residual gas analyzer (MKS e-Vision 2) installed on the pre-lens stage of the energy analyzer. The pressure in the NAP cell was measured with a gas-independent capacitance gauge (CMR361, Pfeiffer Vacuum). An e-beam heater was placed on the back of the NAP cell, allowing sample heating up to 600 K. After each sample loading, the position of the sample was optimized to maximize the intensity of the signal. For all core level regions, a pass energy of 20 eV was used. As the samples were conductive, no charge compensation was required. For all clean samples (before NAP-XPS measurements), the valence band (VB) region spectra were also measured for energy scale calibration with Fermi-edge. The XPS spectra were analyzed with CasaXPS software after Shirley or linear type background subtraction. Symmetric peaks were fitted using a Gaussian/Lorentzian product formula with suitable G/L ratios, and asymmetric peaks were fitted with the three-parameter Lorentzian asymmetric line shape. For quantitative analysis, Scofield relative sensitivity factors (RSFs) were used for correcting the peak areas [22]. The coverage of In was estimated using Equation (1) [23] based on quantification of XPS results.

$$\frac{I_o}{I_s} = \frac{I_o^\infty}{I_s^\infty} \frac{1 - \exp(-t/\lambda_{in}^l(E_o)\cos\theta)}{\exp(-t/\lambda_{in}^l(E_s)\cos\theta)} \quad (1)$$

where I_o and I_s are the intensities of the In overlayer and the Cu substrate, given by corresponding XPS core-level peak areas corrected by the RSFs. I_o^∞ and I_s^∞ are the signal intensities for infinitely thick layer of In and Cu, respectively. $\lambda_{in}^l(E_o)$ and $\lambda_{in}^l(E_s)$ are the inelastic mean free path of the photoelectrons moving through the In layer with energies E_o and E_s, obtained from the NIST Electron Inelastic-Mean-Free-Path Database [24]. θ is the photoelectron emission angle and t is the thickness of In overlayer.

3. Results and discussion

3.1. Surface properties of In/Cu model catalysts

To investigate the interactions between Cu and In, we first prepared four model samples with varied coverage of In from 0.2 to 2.0 monolayer (ML) on Cu foil, along with pure Cu and In foils as references. The SEM images (Fig. S1) show that, by means of e-beam evaporation, In initially (0.2 ML) aggregated on the defective edge of the Cu surface, and did not present on the flat surface. As the In coverage increases to 0.9 ML, In nanoparticles can be observed on the flat surface but still distribute mainly on the slightly grooved areas (formed during the electrochemical polishing). On the sample with 1.4 ML In, In nanoparticles are homogeneously distributed. With further increase of In coverage up to 2.0 ML, the In domains interconnected with each other. This growth behavior is similar to that of many other bimetallic systems [25–27]. Fig. 1 shows the Cu $2p_{3/2}$ and In $3d_{5/2}$ XPS spectra from the Cu, In and In/Cu surfaces taken at room temperature under UHV. With the increase in the amount of deposited In, the binding energy (BE) of the Cu $2p_{3/2}$ peaks gradually increased from 932.7 eV for Cu foil to 933.06 eV for the sample with 2.0 ML In (Fig. 1a). The primary LMM Auger transition of Cu, which originates from the $3d^8$ configuration due to a single L_3 ($2p_{3/2}$) core-hole decay involving two M_{45} (3d) electrons [28], is shown in Fig. 1c. The final state splitting components, namely ^3F, ^1D, ^1G and ^1S, can be clearly identified, while the ^3P is not visible due to its low intensity. Furthermore, another Auger peak arising from the $L_2L_3M_{45}$ Coster-Kronig transitions is also observed [29]. Because we did not observe any O 1s peak after the In deposition (Fig. S2), and the peak shape of Cu 2p and Cu LMM Auger peaks (Fig. 1a and c) remained the same as those of metallic Cu, we can exclude the oxidation of Cu as the reason for the BE shift. In

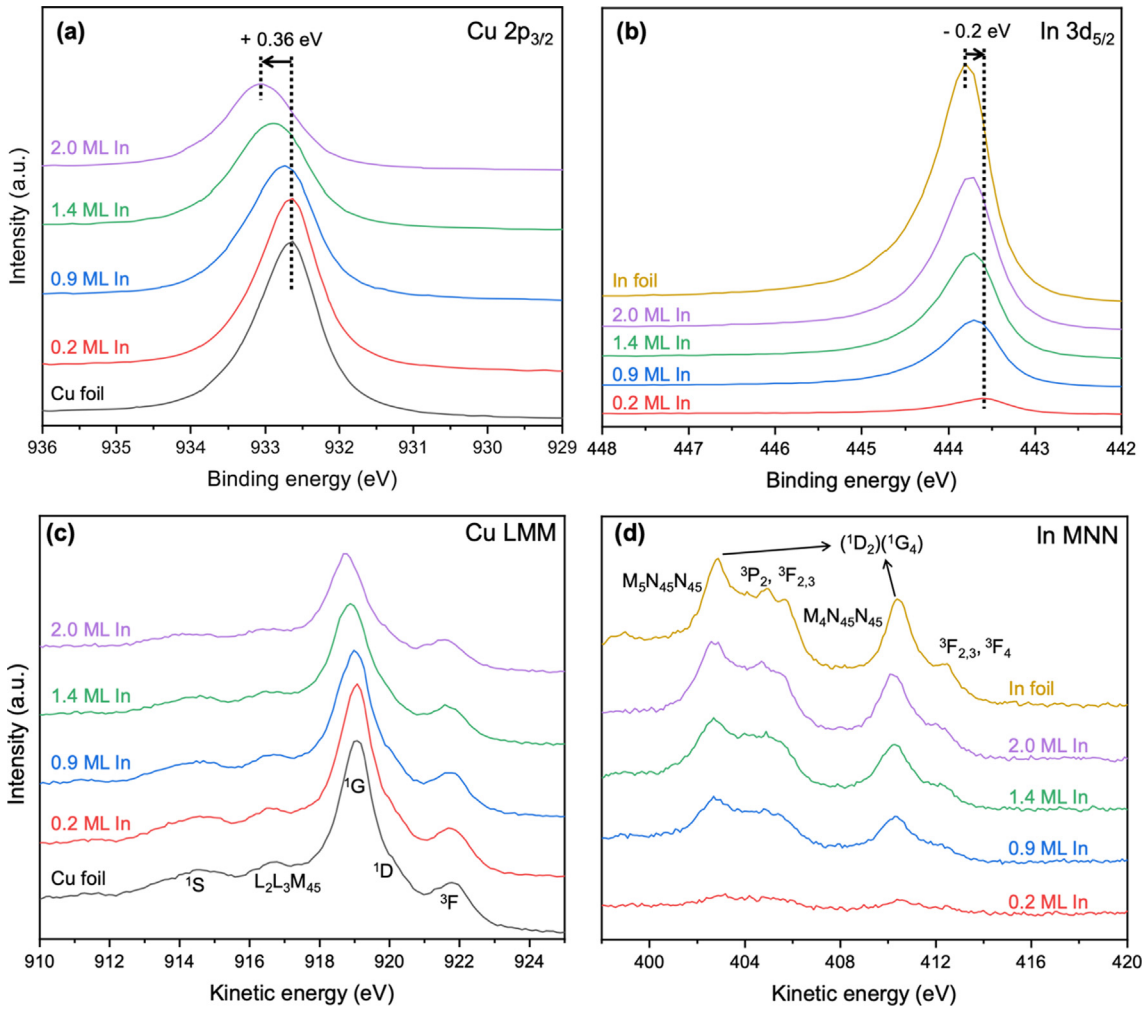

Fig. 1. (a, b) XPS spectra of the Cu $2p_{3/2}$, In $3d_{5/2}$ regions and (c, d) X-ray excited Cu LMM and In MNN Auger peaks of Cu foil, In foil, and In/Cu samples with different surface In coverage. Spectra are unsmoothed data. The In coverage is indicated by monolayer (ML) calculated from the peak area ratio of In $3d_{5/2}$ and Cu $2p_{3/2}$ after a Shirley type background subtraction and correction by the corresponding RSFs.

accordance with the results in Fig. 1a, b shows that decreasing the amount of In leads to a decrease in the BEs of In $3d_{5/2}$: from 443.8 eV for pure In foil to 443.6 eV for 0.2 ML In on Cu. In addition, the valence band spectra (Fig. S3) show the variation of the density of states (DOS) for Cu with different In coverages compared to the pure elements. The Cu d band peak shifts gradually from 2.8 eV to 3.2 eV with the increase of In coverage. This trend is similar to that of the Au-In and Au-Sn alloys systems and has been suggested as the result of the s-d hybridization of the s and d orbitals of Au with s and p orbitals of the main-group atoms upon alloying [30,31]. These results, along with the observations in the core-level BE shifts, can confirm the formation of Cu-In alloys. Although this phenomenon was not reported for Cu-In samples, the BE shifts of the Pd and In peaks due to the formation of Pd-In alloys have been observed [32]. Additionally, one may also notice that the bulk plasmon loss peak associated with the In $3d_{5/2}$ core level at ~455.5 eV (Fig. S4) of the pure In sample [33,34] does not exist on any In 3d spectra of the In/Cu samples. This implies that In exists in a highly dispersed form after deposition on Cu, which further supports the formation of Cu-In alloy. The In MNN Auger peaks in Fig. 1d result from two different final states with a $4d^8$ configuration, namely M_5 ($3d_{5/2}$) and M_4 ($3d_{3/2}$) core-hole decay involving two N_{45} (4d) electrons. Both Auger transitions consist of one strong line corresponding to the $(^1D_2)(^1G_4)$ electron configuration and weak asymmetric peaks on the high energy side [35]. The weak peaks in the $M_5N_{45}N_{45}$ line can be assigned to $^3P_2$ and $^3F_{2,3}$ configurations, while in the $M_4N_{45}N_{45}$ line, the can be assigned to $^3F_{2,3}$ and $^3F_4$ configurations [35]. Similar to Cu, the shape of the In MNN Auger peaks remains unchanged for all samples, further confirming the metallic state of In.

To qualitatively interpret the relative BE shifts with the change in In surface coverage, a simple charge transfer model of Cu-In coordination near the surface is proposed (Fig. 2). With the deposition of In, Cu was more positively charged in the In-coordinated state relative to the "pure Cu" state and thus showed an increased Cu 2p BE. In turn, increasing the In coverage resulted in the decreased ratio of Cu-In coordination, thus the In 3d BE value of high In coverage sample approached that of the In foil. This model indicates that the formation of Cu-In surface alloy induces a flow of electrons from Cu to In. Notably, the electronegativity of Cu (1.90) is slightly higher than that of In (1.78), therefore electron flow from In to Cu is expected. Such counterintuitive results were explained earlier by Goodman *et al.*: the charge transfer in surface alloys can be contrary to that of bulk alloys due to the anisotropic character of a surface that changes the relative electronegativities of metal atoms [36]. Furthermore, the BE shifts of surface alloys can also be influenced by other factors during the photoelectron emission process. For example, the geometric contribution

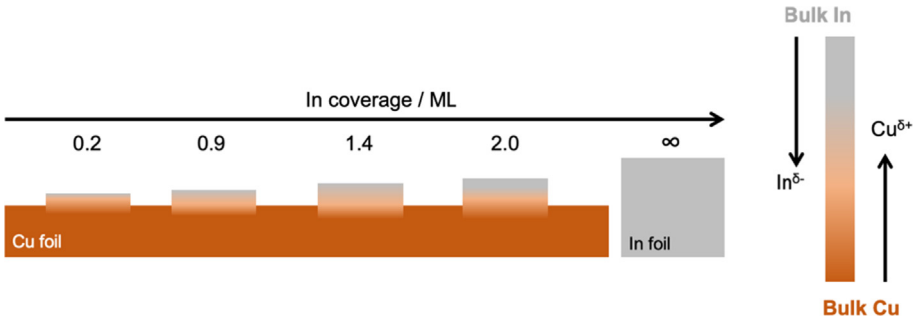

Fig. 2. Schematic illustration of the Cu-In charge transfer model for Cu-In alloying on Cu foil surface.

caused by lower effective coordination of surface adlayer than the bulk material could decrease the BE of the adlayer element [37], orbital rehybridization may decrease the BEs of both adlayer and substrate elements [38,39], and the final state effects partially cancel the abovementioned initial state contributions [40,41]. Overall, these factors lead to the observed BE shifts of Cu and In.

3.2. NAP-XPS in the presence of CO_2 at 300 K

Next we exposed the clean Cu, In and In/Cu surfaces to 0.2 mbar CO_2 at 300 K to investigate the effect of CO_2 on the surface properties. The Cu $2p_{3/2}$ and In $3d_{5/2}$ spectra collected from the different surfaces are shown in Fig. 3a and b. Compared with the spectra obtained under UHV, introducing CO_2 did not change the peak shape of Cu $2p_{3/2}$ (Fig. 3a) or Cu LMM (Fig. S5a), indicating that Cu can maintain its metallic state [42]. In contrast, the peak shape of In $3d_{5/2}$ was significantly changed upon CO_2 exposure: additional peaks contributed by In oxides can be observed at a higher BE (Fig. 3b). The deconvolution of the In $3d_{5/2}$ region using a multi-peak fitting indicates that the fraction of the oxidized In is dependent on the amount of deposited In. As shown in Fig. 3b, a small amount of In (0.2 ML) was completely oxidized, whereas the

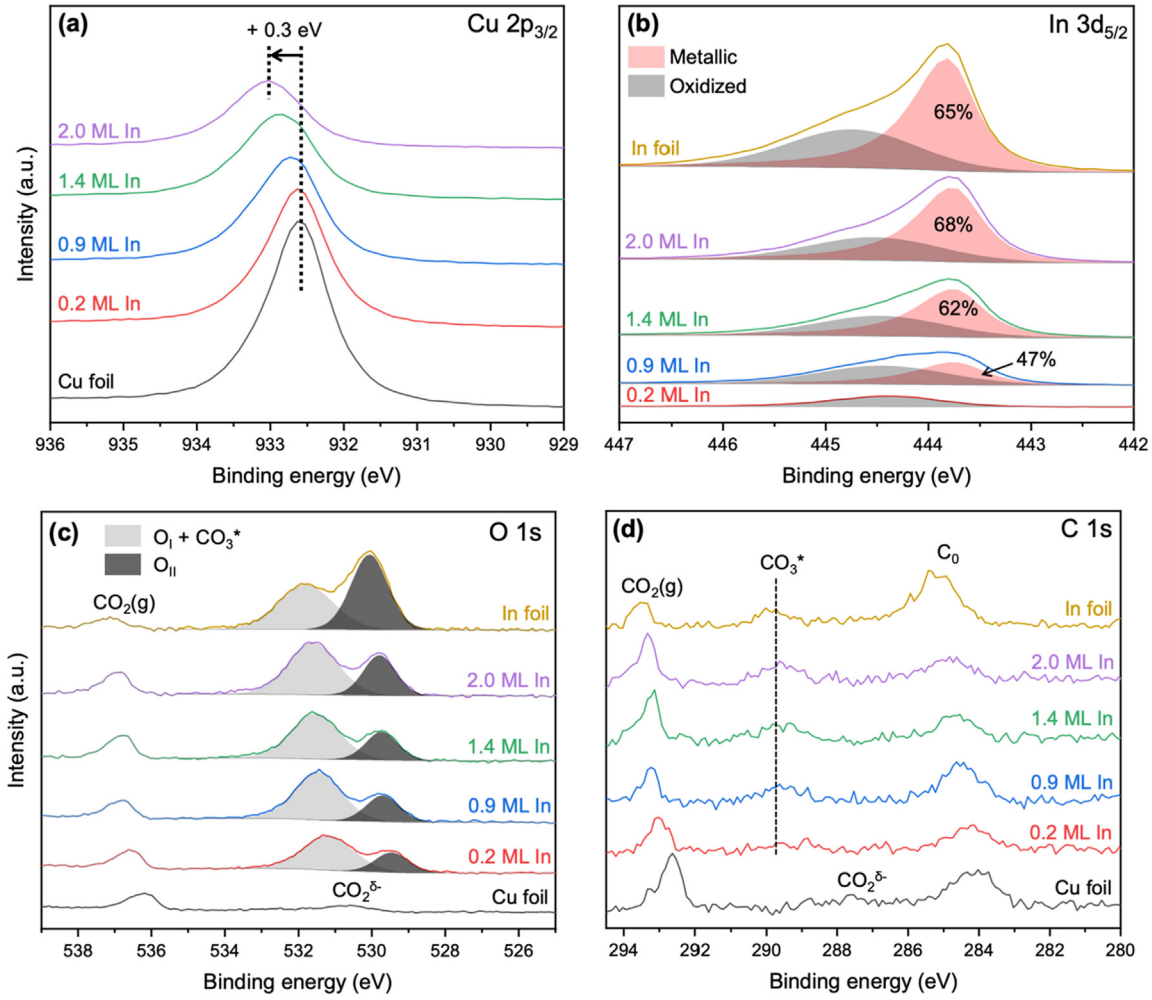

Fig. 3. NAP-XPS spectra of the (a) Cu $2p_{3/2}$, (b) In3 $d_{5/2}$, (c) O 1s, and (d) C 1s regions of Cu foil, In foil, and In/Cu samples with different surface In coverage upon exposure to 0.2 mbar CO_2 at 300 K.

increased deposition amount of In led to an increase in the remaining ratio of metallic In from ~47% for the 0.9 ML In sample to ~65% for the In foil sample. Meanwhile, the Auger peaks in Fig. S5b also exhibited hybridized characteristics of metallic and oxidized In [43]. Notably, as In is oxidized by CO_2, the In concentration in the Cu-In alloy should be smaller than that before CO_2 introduction. Such a phase separation can be confirmed by the slight shift in the Cu $2p_{3/2}$ peak to a lower BE (Fig. 3a). Nevertheless, the metallic phase of Cu and In remains to be alloyed, as the peak shifts of Cu $2p_{3/2}$ to a higher BE and In $3d_{5/2}$ to a lower BE compared with the pure metal references are consistent with the results from UHV measurement. Together, these results indicate that at room temperature, Cu can maintain its metallic state upon CO_2 exposure while In can be partially oxidized, leading to the partial dealloying of Cu-In alloys.

Apart from the surface properties of In/Cu samples, we also monitored the adsorption states of CO_2. Fig. 3c and d shows a series of C 1s and O 1s spectra collected from different surfaces at 300 K under 0.2 mbar CO_2. Gas-phase CO_2 was clearly detected in the O 1s region (~536.5 eV) and C 1s region (~293.0 eV). In C 1s region, an additional peak can be observed at ~284.5 eV for all five samples, and is assigned to neutral carbon impurity (C_0) as this peak also appears after the sample is placed in NAP cell without exposure to any gases (Fig. S6) [44]. Here, the slight variation in the positions of gas-phase CO_2 and C_0 peaks on different samples is due to the change of sample work function and vacuum level after In alloying with Cu. As the gas phase is not electrically contacted with the sample surface and the energy analyzer, its energy scale is referenced to the vacuum level of the gas ($E_{vac\text{-}gas}$), which is between the vacuum level of the sample and the aperture [45]. Besides, the sample position, which also affects the gas-phase peak position [45], was optimized individually for each measurement. Thus, the gas-phase peak positions are different for samples with different In coverage. Similarly, the C_0 peak positions are also dependent on the work function of the sample and vary for different samples [46]. As we tried to use identical sample position in each experiment, the these peaks shifted systematically as In coverage increases. On the Cu foil surface, a weak peak at ~288.0 eV can be observed in addition to the C_0 peak. This peak can be assigned to the chemisorbed, negatively charged CO_2 [47]. In contrast, an additional peak at 289–290 eV can be observed for the samples containing In. This peak is assigned to the adsorbed CO_3 according to previous studies [42,44,47,48]. Thus, the different adsorption species on Cu and In/Cu samples clearly indicates that the deposition of In changes the activation mechanism of CO_2.

In the O 1s region, the Cu foil sample shows a weak peak at ~530.5 eV, which corresponds to the chemisorbed CO_2. However, for the In-containing samples, high-intensity doublet O 1s peaks are observed at 528–534 eV. The double O 1s peaks are characteristic of indium oxides and common for oxides with cations in multiple valence states [49–51]. This spectrum can be deconvoluted into two peaks: a lower BE peak at 529.8 eV, assigned to the lattice oxygen of In_2O_3 (O_{II}), and a higher BE one at 531.5 eV, assigned to the defective In_2O_{3-x} (O_I). The higher BE of O_I relative to O_{II} can be well explained by the fact that oxygen vacancies change the distribution of the negative charge density [52].

Here, it should be noted that the O 1s peak from carbonate overlaps with that from the O_I species of indium oxides. Thus, the peaks at ~531.4 eV in Fig. 3c are contributed by the oxygen from both O_I species and carbonate. To identify the ratio of oxygen species, the contribution of carbonate to the O 1s peak at ~531.4 eV was calculated from the area of the C 1s peak at ~289.5 eV using the C:O ratio of 1:3 and the corresponding RSFs for all In/Cu and In foil samples, respectively. The calculated O_I/O_{II} ratio is shown in Fig. 4a. Obviously, a decreasing trend in the O_I/O_{II} ratio is observed with an increase of In coverage, and the In foil sample corresponds to the lowest fraction of oxygen vacancies. The ratios of C 1s peak area contributed by carbonate, and the O_I peak area for all samples are also compared in Fig. 4a. With the lowest O_I/O_{II} ratio, the In foil sample adsorbs the least amount of CO_2 in the form of carbonate. In contrast, all In/Cu samples show a CO_3/O_I ratio at least 1.5 time higher than that of the In foil sample, and the highest CO_3/O_I ratio is observed for the sample with 1.4 ML of In. These results imply that, compared with In, the Cu-In alloy also enhances the adsorption of CO_3 on the In_2O_{3-x} surface.

To further investigate the oxidation behavior of In/Cu samples, additional NAP-XPS measurements were taken for the In/Cu sample with 1.4 ML In and In foil under 0.2 mbar O_2 at 300 K, and the corresponding In 3d and O 1s spectra are shown in Fig. S7. Fig. 4b shows that for both In/Cu and In foil samples, the fraction of oxidized In calculated from the In $3d_{5/2}$ spectra is higher in O_2 than in CO_2, as O_2 is a much stronger oxidant. Moreover, the ratio of defective oxygen (O_I) species is higher than lattice oxygen (O_{II}) in CO_2 (Fig. 4b). Overall, we conclude that CO_2 tends to oxidize In with a relatively high fraction of oxygen vacancies and this effect is more distinct on Cu-In alloy than pure In.

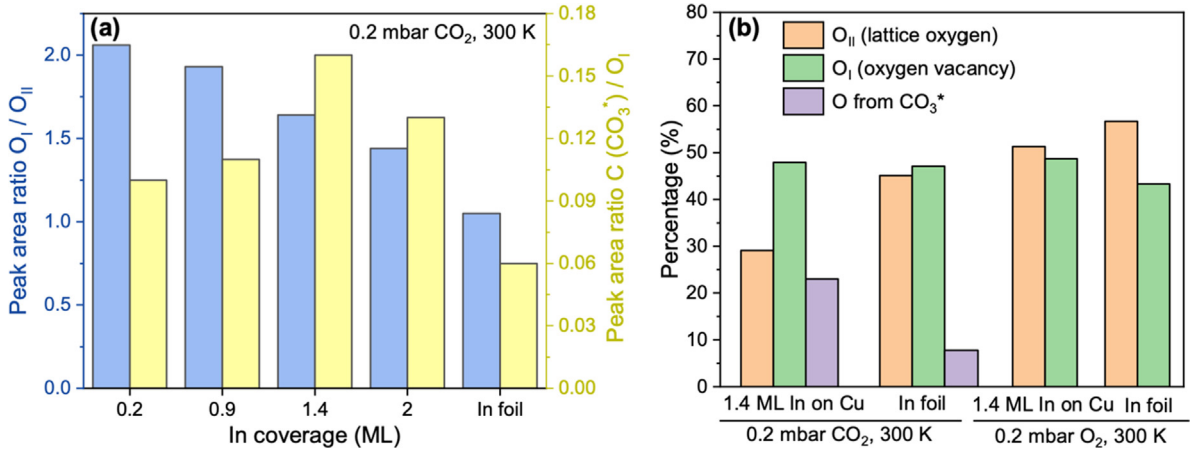

Fig. 4. (a) Peak area ratios of defective/lattice oxygen (O_I/O_{II}) and carbon from the contribution of carbonate/defective oxygen (C from CO_3^*/O_I) for In/Cu and In foil samples upon exposure to 0.2 mbar CO_2 at 300 K, and (b) percentage of different oxygen species (O_{II}, O_I, and O from CO_3^*) in O 1s region of one In/Cu sample with 1.4 ML In and In foil upon exposure to 0.2 mbar CO_2 or O_2 at 300 K.

3.3. NAP-XPS under CO_2 hydrogenation conditions at 300–600 K

Providing the essential information on the interaction between the CO_2 and In/Cu surfaces, we further investigated the evolution of the chemical states of Cu and In, as well as the surface O and C species under CO_2 hydrogenation conditions. Fig. S1 shows that the 1.4 ML In samples exhibits the most homogeneous In particle distribution on Cu foil and the highest particle density (1.4×10^{10} cm^{-2}) compared with other In/Cu samples (Fig. S1), offering the highest Cu-In interface area. Thus, the In/Cu sample with 1.4 ML In was used for the following study. The spectra were acquired under 0.2 mbar CO_2, or the mixture of 0.2 mbar CO_2 and 0.6 mbar H_2, at 300, 450, and 600 K, respectively.

The evolution of Cu $2p_{3/2}$ BE upon exposure to CO_2 and CO_2 + H_2 at different temperatures is shown in Fig. 5a and d, respectively. Obviously, as the temperature increases, the position of the Cu $2p_{3/2}$ peak shifts to a lower BE by ~0.3 eV (from 300 K under UHV to 600 K with gases), which is independent of the gas atmosphere. As discussed earlier, the BE shift can be attributed to the de-alloying of the Cu-In alloy due to the oxidation of In (Fig. S7a and b). As confirmed in Fig. 5b and e, the In is progressively oxidized from 100% metallic In (under the UHV condition at 300 K) to 100% In_2O_{3-x} (under CO_2 and CO_2 + H_2 conditions at 600 K). This trend is further confirmed by the change in the In MNN Auger peaks (Fig. S8c and d). It is necessary to note that the existence of H_2 in the gas atmosphere did not influence the oxidation of In by CO_2 (Fig. 5e and f). The reduction of In_2O_3 powder by 1.0 bar H_2 has been reported to be limited to the surface without any detectable structural change below 500 K, and a deep reduction to metallic In was observed above 573 K [53]. It was also reported that the reduction of In_2O_3 layer on metallic In was as slow as 1 nm/h at 623 K in 40 mbar H_2 [54]. With H_2 partial pressure of 0.6 mbar and the co-existence of CO_2 in this work, it is reasonable that the kinetics of oxidation by CO_2 would prevail over the reduction by H_2, resulting in less metallic In at 450 K, and no metallic In left at 600 K upon exposure to CO_2/H_2 mixture. In addition, the SEM image (Fig. S9a) of the In/Cu sample with 1.4 ML In coverage was also taken after exposure to the CO_2/H_2 mixture at 600 K. In the particle size distribution histogram of samples before and after exposure the CO_2/H_2 mixture at 600 K (Fig. S9b), no significant sintering of In nanoparticles is observed, thus the influence of the slow diffusion of gas in large particles can be excluded.

Fig. 5c and f show that with the increase in temperature, a clear increasing trend of the O_{II}/O_I peak ratio, together with an overall building of the O 1s peaks can be observed. The relative intensities of O_I and O_{II} peaks are summarized in Table 1. Meanwhile, it should

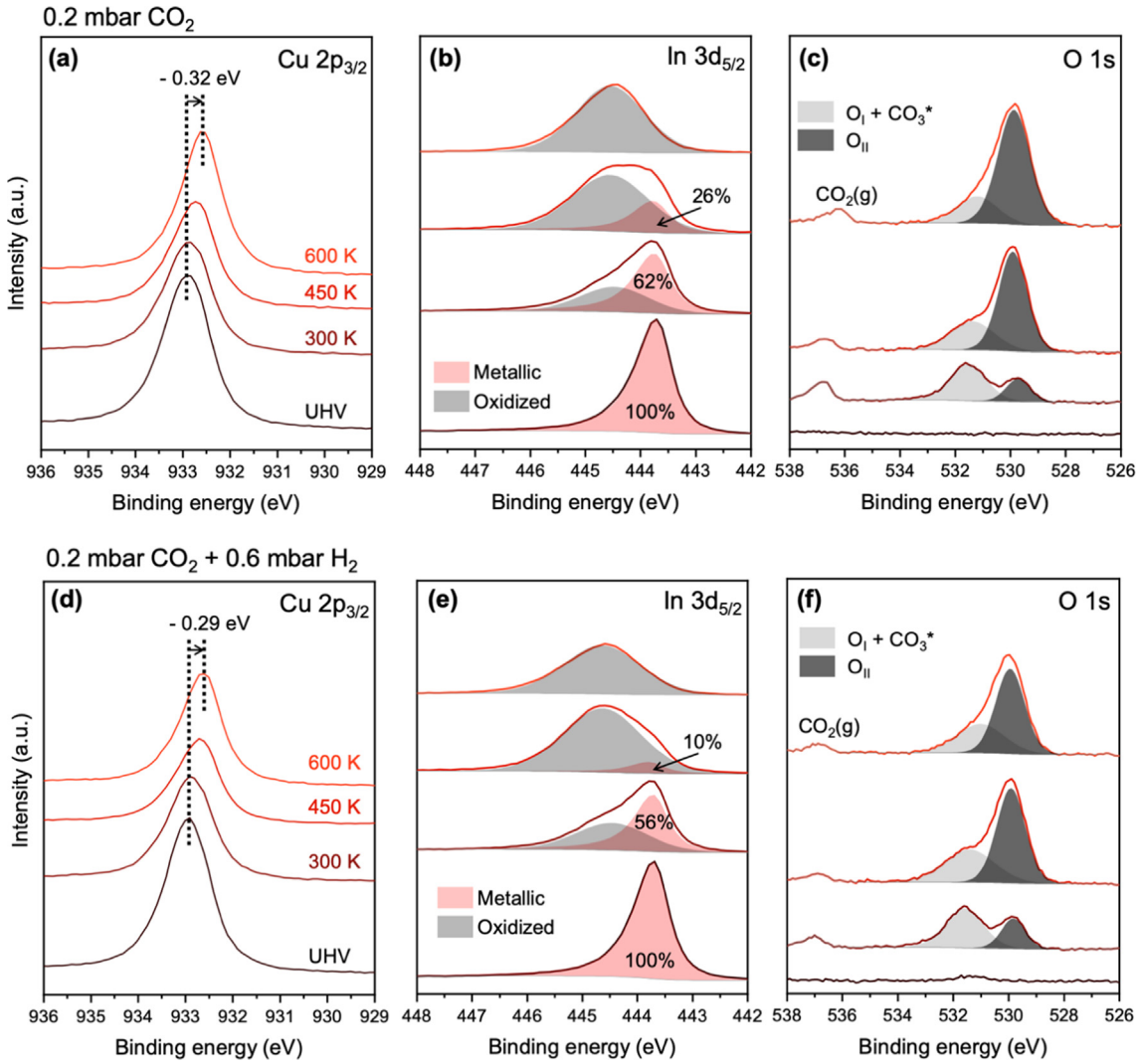

Fig. 5. Comparison of NAP-XPS spectra of (a, d) Cu $2p_{3/2}$, (b, e) In $3d_{5/2}$, and (c, f) O 1s regions for the In/Cu sample with 1.4 ML In coverage upon exposure to 0.2 mbar CO_2 (a, b, and c) and the mixture of 0.2 mbar CO_2 + 0.6 mbar H_2 (d, e, and f) at 300–600 K. Spectra are unsmoothed data.

Table 1
Positions and relative intensities of different O 1s species on the In/Cu sample with 1.4 ML In coverage under different conditions.

Gases	Temperature (K)	Positions (eV) and relative intensities				
		$O_I + CO_3^*$	O_I	CO_3^*	O_{II}	
CO_2	300	531.5	63%	8%	529.7	29%
	450	531.4	29%	2%	529.9	69%
	600	531.2	22%	0%	529.9	78%
$CO_2 + H_2$	300	531.6	63%	4%	529.8	33%
	450	531.4	35%	3%	529.9	62%
	600	531.0	36%	0%	530.0	64%

be pointed out that at 600 K, even though all the In on the sample surface is oxidized, O_I still accounts for 22% (for CO_2 exposure) or 36% (for CO_2 + H_2 exposure) of the O 1s peaks. This means that the oxygen vacancies on the In/Cu sample are stable at up to 600 K upon exposure to CO_2 and CO_2 + H_2, and thus, can function as the active sites for CO_2 activation under such conditions. In addition, it can also be observed that with the increase in temperature, the fraction of O 1s peak area contributed by carbonate adsorbed on the sample surface (Table 1 and C 1s region in Fig. S10) decreases. By comparing the relative intensities of O_I and CO_3 under different atmospheres, it is also obvious that the mixture of CO_2 and H_2 leads to a higher fraction of oxygen vacancies and a lower fraction of carbonates than pure CO_2, indicating that the reduction atmosphere may preserve more oxygen vacancies, and that H_2 may react with adsorbed carbonates to form CO_2 hydrogenation products. In Fig. S10, it is shown that the carbon deposition is substantially higher when the sample is exposed to CO_2/H_2 mixture at 600 K, which can be attributed to (1) longer heating time due to the existence of highly thermal conductive gas H_2 and (2) formation of carbon from the reduction of CO_2 by H_2 [44,47,55]. Other intermediates of CO_2 hydrogenation, such as HCOO*, HCO*/H_2CO*, and CH_3O groups have been previously observed using synchrotron-based NAP-XPS [44,47,48,56]. Although we could also deconvolute our C 1s region to identify these intermediates based on previous studies (Fig. S11), it should be noted that a reliable peak fitting for C 1s region should be in consistent with the O 1s region counterpart, which is not realistic in this work as the majority of O 1s region species are from metal oxides and the contribution of carbon species is as small as 2–3%. Thus, details of other CO_2 hydrogenation intermediates are not discussed as we try not to overinterpret the results.

4. Discussion

In this work, we investigated the reactivity of CO_2 on In/Cu samples with different In coverages on Cu foil, as well as on polycrystalline Cu and In foils. By means of e-beam evaporation, the In readily formed a surface alloy with the polycrystalline Cu substrate. This is an ideal model catalyst as the formation of Cu-In alloys is widely observed in different Cu-In bimetallic catalysts. However, as soon as CO_2 was introduced onto the sample, In was oxidized and consequently de-alloyed from the Cu-In alloy (Figs. 3 and S4). Under the same conditions, Cu remained in a metallic state, in agreement with the recent NAP-XPS and NEXAFS studies on Cu foil and Cu single crystals [42,57]. The selective oxidation of In is consistent with the fact that In_2O_3 (ΔH_f° = −923.5 kJ/mol) is thermodynamically more stable than CuO (ΔH_f° = −56.06 kJ/mol) or Cu_2O (ΔH_f° = −170.71 kJ/mol) under standard conditions [58,59]. Meanwhile, we observed O 1s peaks from both defective and lattice oxygen atoms of the indium oxide, and the ratio of defective oxygen was much higher for the indium oxides from In/Cu samples than that from the In foil, which agrees well with previous observations that oxygen vacancies tend to be concentrated on the topmost surface layers of In_2O_3, rather than in the bulk [60,61]. According to the theoretical and experimental studies, defective In_2O_{3-x} sites are prone to activate CO_2 and assist the hydrogenation [4,8]. With NAP-XPS, we observed the formation of more defective In_2O_{3-x} sites on In/Cu than on In surfaces upon CO_2 exposure. Such findings from our In/Cu model catalysts may partially explain the previous observations that Cu-In catalysts show better performance than pure In-based catalysts [12–14].

Next, the activation of CO_2 on Cu, In, and In/Cu surfaces at 300 K are discussed. On the polycrystalline Cu surface, we observed negatively charged, chemisorbed $CO_2^{\delta-}$ from both O 1s and C 1s regions (Fig. 3c and d), which is in agreement with the widely reported chemisorption of CO_2 as the initial activation step on polycrystalline Cu [47], as well as on Cu(1 1 1) surfaces [48,57,62]. However, the further reaction between CO_2 and $CO_2^{\delta-}$ which leads to the formation of carbonate was not observed in our experiments, nor were the results from Ren et al. [62], possibly due to the relatively slow reaction rate [47]. In contrast, on the In/Cu and polycrystalline In surfaces, a substantial build-up of carbonate peak were observed (Fig. 3d). According to previous DFT studies on CO_2 adsorption on the In_2O_3 surface, CO_2 is activated in the form of carbonate upon adsorption by combining with surface oxygen on O-In-O sites with low coordination numbers of their constituent atoms [9]. This theoretically explained our observation from NAP-XPS measurements that the oxygen vacancies from In_2O_{3-x} sites directly corresponded to the formation of carbonate. In addition, the depletion of $CO_2^{\delta-}$ peaks implies that the In_2O_{3-x} sites may also facilitate the stabilization of the carbonate originating from $CO_2^{\delta-}$ on the Cu surfaces, similar to the function of ZnO sites [44,47]. Overall, our NAP-XPS results demonstrate experimentally the activation of CO_2 on In/Cu surfaces and the importance of defective In_2O_{3-x} sites for CO_2 hydrogenation.

In addition, on In/Cu samples, the density of carbonate adsorbed on oxygen vacancies is increased by at least a factor of 1.5 compared with In foil (Fig. 4a). This indicates a potential synergy between the Cu-In alloy and In_2O_{3-x} sites, where CO_2 tends to be more easily activated on the oxygen vacancies adjacent to the Cu-In alloy sites (*i.e.*, on the boundaries between Cu-In alloys and In_2O_{3-x}). Such a synergy can be further supported by the peak area ratio of $C(CO_3^*)/O_I$ on the different In/Cu samples shown in Fig. 4a. Although it is difficult to obtain a precise particle density for the sample with 0.9 ML In due to the inhomogeneous particle distribution, we estimated a particle density ranging from 9.2×10^8 to 2.9×10^9 cm^{-2} for this sample from several representative SEM images. While for the 1.4 ML In sample the particle density is around 1.4×10^{10} cm^{-2}. Thus, the $C(CO_3^*)/O_I$ ratio increases and reaches its maximum at 1.4 ML In coverage, as the highest density of In_2O_{3-x}/Cu-In sites is expected. However, a further increase in the In coverage to 2.0 ML leads to a continuous In overlayer (Fig. S1), resulting in a decreased $C(CO_3^*)/O_I$ ratio. Previously, Shi *et al.* prepared a $Cu_{11}In_9$-In_2O_3 catalyst with superior activity and selectivity for CO_2 hydrogenation to methanol, and proposed that $Cu_{11}In_9$ interacts closely with In_2O_3 and thus affects the adsorption strength of CO_2 [13]. Similarly, the CO_2-TPD results from Gao et al. also suggested that Cu-In alloy corresponds to additional CO_2

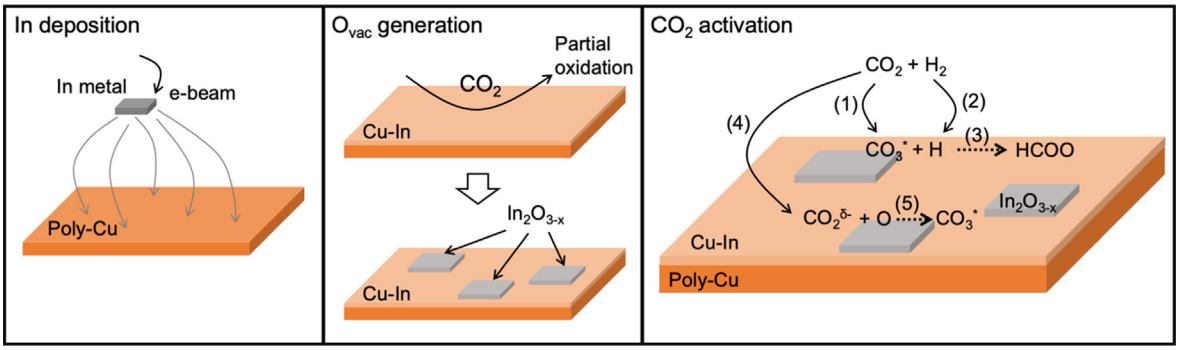

Fig. 6. Schematic illustration of the formation of Cu-In alloy, the partial oxidation of In/Cu surface to In_2O_{3-x} with oxygen vacancies, and the activation of CO_2 on the In_2O_{3-x}/Cu-In boundaries and proposed further hydrogenation as an initial step for methanol production.

adsorption sites and thus higher methanol selectivity compared with pure Cu or In-based catalysts [14]. In addition, it has also been widely proposed for bimetallic In_2O_3-based catalysts that the metallic (Cu, Pd, Ni or Au) sites provide active hydrogen atoms to the activated CO_2 on In_2O_{3-x} sites so that the initial step of hydrogenation can occur [12,15,16,20,21,63]. Our results not only supports the previous findings but, more importantly, offer direct evidence of the activation of CO_2 on oxygen vacancies and justify the synergy between the Cu-In alloy and the In_2O_{3-x} sites in In_2O_3-based catalysts. These results obtained from In/Cu samples may also be adapted for the purpose of understanding other bimetallic catalysts for CO_2 hydrogenation.

The oxidation state of the In/Cu surfaces and the adsorption of CO_2 change significantly with the gas composition and the temperature, as summarized in Fig. 5 and Table 1. In both CO_2 and CO_2/H_2 mixtures, the metallic In atoms are further oxidized to In_2O_{3-x} at 450 and 600 K, and the quantification of O_I species indicates that oxygen vacancies were preserved under all conditions in our NAP-XPS experiments. However, with the presence of H_2, the In_2O_{3-x} sites were slightly reduced at elevated temperatures, as indicated by the higher ratio of O_I species. In a recent study on an Au/In_2O_3 catalyst, In_2O_3 was also found to be oxidized by CO_2 and partially reduced by H_2, which is consistent with our findings [21]. The reduction of In_2O_3 by H_2 has been found to be limited on the surface at <500 K [53]. Furthermore, the *in operando* XAS-XRD study on In_2O_3 catalyst for CO_2 hydrogenation also considered the reduction by H_2 as a necessary step for catalyst activation due to the formation of oxygen vacancies [11]. Combining the results from published studies on supported catalysts and our In/Cu model system, it can be inferred that oxygen vacancies from In_2O_{3-x} are stable under typical CO_2 hydrogenation conditions, and the reduction process by H_2 can activate the In-based catalyst.

On the basis of the discussion above, a full schematic for the In/Cu phase evolution and the hydrogenation of CO_2 is summarized in Fig. 6. Upon the deposition of In metal on a Cu substrate, In and Cu alloy immediately at the surface. In the presence of CO_2, the Cu-In alloy is partially oxidized with the formation of defective In_2O_{3-x} sites. During CO_2 hydrogenation, both the Cu-In alloy phase and In_2O_{3-x} sites are involved in different reactions. Under CO_2 hydrogenation conditions, the majority of the Cu-In alloy works as the precursor of the highly active In_2O_{3-x} sites, and H_2 dissociates on the remaining Cu-In alloy and metallic Cu. Reaction (1) is the activation of CO_2 to carbonate on the boundary of the In_2O_{3-x} site and Cu-In alloy, and reaction (2) is the adsorption of atomic hydrogen on the Cu-In surface. As the H_2-spliting ability of In_2O_{3-x} is limited [64], the H atoms dissociate from H_2 by Cu and Cu-In alloy sites can spill-over to the adjacent In_2O_{3-x} sites to react with the activated CO_2. This way, further hydrogenation to formate can occur as the initial step for the formation of methanol, which is shown as reaction (3). In addition, reactions (4) and (5) indicate the formation and stabilization of carbonate on the Cu-In alloy surface facilitated by oxygen atoms with low coordination number from the In_2O_{3-x} site. We believe that the combination of the CO_2 activation by oxygen vacancies on the In_2O_{3-x}/Cu-In boundary and the enhanced hydrogen adsorption on In/Cu surface is the potential origin of the superior activity and selectivity of the Cu-In bimetallic catalysts for CO_2 hydrogenation.

5. Conclusions

A series of In/Cu model samples with In coverage from 0.2 to 2.0 ML were prepared on a Cu foil substrate by e-beam evaporation of metallic In. NAP-XPS studies were carried out to understand the evolution of the surface structure and composition as well as solid–gas interactions under CO_2 hydrogenation conditions. After deposition, In was found to form an alloy with the Cu substrate showing clear core-level binding energy shifts. Upon exposure to CO_2 at 300 K, the alloyed Cu-In surface was partially oxidized to In_2O_{3-x}/Cu-In. CO_2 was found to be better activated on the surface In/Cu samples than on the Cu foil reference in the form of carbonate because of the existence of oxygen vacancies on In_2O_{3-x}. The quantification of the carbonate and oxygen vacancies revealed that the Cu-In alloy promoted the utilization of defective In_2O_{3-x} sites for activating CO_2. Further investigations at elevated temperatures up to 600 K and upon exposure to a CO_2/H_2 mixture revealed that 36% of the oxygen species remained as oxygen vacancies and were stable under such conditions. A synergy between Cu-In alloy and oxygen vacancies from In_2O_{3-x} was proposed, in which CO_2 was activated on the In_2O_{3-x}/Cu-In boundaries and further hydrogenated by atomic hydrogen adsorbed on the Cu-In alloy surface. Overall, the obtained results provide fundamental insights into the surface evolution of the In/Cu model catalysts under reaction conditions, and indicate a direct relationship between the existence of surface oxygen vacancies and the enhanced activity of bimetallic Cu-In catalysts for CO_2 hydrogenation.

Declaration of Competing Interest

The authors declare that they have no known competing financial interests or personal relationships that could have appeared to influence the work reported in this paper.

Acknowledgements

This research is supported by Swiss National Science Foundation (Ambizione Project PZ00P2_179989). This research is also part of the activities of SCCER HeE, which is financially supported by Innosuisse-Swiss Innovation Agency. The NAP-XPS system is

funded by the SNSF R'EQUIP project (No. 170736). M.L. acknowledges the Ph.D. scholarship from China Scholarship Council (Grant No. 201506060156).

Appendix A. Supplementary material

Supplementary data to this article can be found online at https://doi.org/10.1016/j.jcat.2021.01.010.

References

[1] A. Züttel, P. Mauron, S. Kato, E. Callini, M. Holzer, J. Huang, Storage of Renewable Energy by Reduction of CO_2 with Hydrogen, Chim. Int. J. Chem. 69 (2015) 264–268, https://doi.org/10.2533/chimia.2015.264.
[2] J. Amouroux, P. Siffert, J. Pierre Massué, S. Cavadias, B. Trujillo, K. Hashimoto, P. Rutberg, S. Dresvin, X. Wang, Carbon dioxide: A new material for energy storage, Prog. Nat. Sci. Mater. Int. 24 (2014) 295–304, https://doi.org/10.1016/j.pnsc.2014.06.006.
[3] International Energy Agency, World Energy Outlook 2016, Head of Communication and Information Office, France, 2016. https://webstore.iea.org/world-energy-outlook-2016.
[4] K. Sun, Z. Fan, J. Ye, J. Yan, Q. Ge, Y. Li, W. He, W. Yang, C. Liu, Hydrogenation of CO_2 to methanol over In_2O_3 catalyst, J. CO_2 Util. 12 (2015) 1–6, https://doi.org/10.1016/j.jcou.2015.09.002.
[5] O. Martin, A.J. Martín, C. Mondelli, S. Mitchell, T.F. Segawa, R. Hauert, C. Drouilly, D. Curulla-Ferré, J. Pérez-Ramírez, Indium Oxide as a Superior Catalyst for Methanol Synthesis by CO_2 Hydrogenation, Angew. Chem. Int. Ed. 55 (2016) 6261–6265, https://doi.org/10.1002/anie.201600943.
[6] M.S. Frei, M. Capdevila-Cortada, R. García-Muelas, C. Mondelli, N. López, J.A. Stewart, D. Curulla Ferré, J. Pérez-Ramírez, Mechanism and microkinetics of methanol synthesis via CO_2 hydrogenation on indium oxide, J. Catal. 361 (2018) 313–321, https://doi.org/10.1016/j.jcat.2018.03.014.
[7] S. Dang, B. Qin, Y. Yang, H. Wang, J. Cai, Y. Han, S. Li, P. Gao, Y. Sun, Rationally designed indium oxide catalysts for CO_2 hydrogenation to methanol with high activity and selectivity, Sci. Adv. 6 (2020) eaaz2060, https://doi.org/10.1126/sciadv.aaz2060.
[8] J. Ye, C. Liu, D. Mei, Q. Ge, Active Oxygen Vacancy Site for Methanol Synthesis from CO_2 Hydrogenation on In_2O_3(110): A DFT Study, ACS Catal. 3 (2013) 1296–1306, https://doi.org/10.1021/cs400132a.
[9] J. Ye, C. Liu, Q. Ge, DFT Study of CO_2 Adsorption and Hydrogenation on the In_2O_3 Surface, J. Phys. Chem. C 116 (2012) 7817–7825, https://doi.org/10.1021/jp3004773.
[10] W. Wang, Y. Zhang, Z. Wang, J. Yan, Q. Ge, C. Liu, Reverse water gas shift over In_2O_3–CeO_2 catalysts, Catal. Today 259 (2016) 402–408, https://doi.org/10.1016/j.cattod.2015.04.032.
[11] A. Tsoukalou, P.M. Abdala, D. Stoian, X. Huang, M.-G. Willinger, A. Fedorov, C.R. Müller, Structural Evolution and Dynamics of an In_2O_3 Catalyst for CO_2 Hydrogenation to Methanol: An Operando XAS-XRD and In Situ TEM Study, J. Am. Chem. Soc. 141 (2019) 13497–13505, https://doi.org/10.1021/jacs.9b04873.
[12] Z. Shi, Q. Tan, D. Wu, A novel Core-Shell structured CuIn@SiO_2 catalyst for CO_2 hydrogenation to methanol, AIChE J. 65 (2019) 1047–1058, https://doi.org/10.1002/aic.16490.
[13] Z. Shi, Q. Tan, C. Tian, Y. Pan, X. Sun, J. Zhang, D. Wu, CO_2 hydrogenation to methanol over Cu-In intermetallic catalysts: Effect of reduction temperature, J. Catal. 379 (2019) 78–89, https://doi.org/10.1016/j.jcat.2019.09.024.
[14] J. Gao, F. Song, Y. Li, W. Cheng, H. Yuan, Q. Xu, Cu_2In nanoalloy enhanced performance of Cu/ZrO2 catalysts for the CO_2 hydrogenation to methanol, Ind. Eng. Chem. Res. (2020), https://doi.org/10.1021/acs.iecr.9b06956.
[15] L. Yao, X. Shen, Y. Pan, Z. Peng, Synergy between active sites of Cu-In-Zr-O catalyst in CO_2 hydrogenation to methanol, J. Catal. 372 (2019) 74–85, https://doi.org/10.1016/j.jcat.2019.02.021.
[16] N. Rui, Z. Wang, K. Sun, J. Ye, Q. Ge, C. Liu, CO_2 hydrogenation to methanol over Pd/In_2O_3: effects of Pd and oxygen vacancy, Appl. Catal. B Environ. 218 (2017) 488–497, https://doi.org/10.1016/j.apcatb.2017.06.069.
[17] A. García-Trenco, A. Regoutz, E.R. White, D.J. Payne, M.S.P. Shaffer, C.K. Williams, PdIn intermetallic nanoparticles for the Hydrogenation of CO_2 to Methanol, Appl. Catal. B Environ. 220 (2018) 9–18, https://doi.org/10.1016/j.apcatb.2017.07.069.
[18] M.S. Frei, C. Mondelli, R. García-Muelas, K.S. Kley, B. Puértolas, N. López, O.V. Safonova, J.A. Stewart, D.C. Ferré, J. Pérez-Ramírez, Atomic - scale engineering of indium oxide promotion by palladium for methanol production via CO_2 hydrogenation, Nat. Commun. 10 (2019) 1–11, https://doi.org/10.1038/s41467-019-11349-9.
[19] J.L. Snider, V. Streibel, M.A. Hubert, T.S. Choksi, E. Valle, D.C. Upham, J. Schumann, M.S. Duyar, A. Gallo, F. Abild-Pedersen, T.F. Jaramillo, Revealing the Synergy between Oxide and Alloy Phases on the Performance of Bimetallic In–Pd Catalysts for CO2 Hydrogenation to Methanol, ACS Catal. (2019) 3399–3412, https://doi.org/10.1021/acscatal.8b04848.
[20] X. Jia, K. Sun, J. Wang, C. Shen, C. Liu, Selective hydrogenation of CO_2 to methanol over Ni/In2O3 catalyst, J. Energy Chem. 50 (2020) 409–415, https://doi.org/10.1016/j.jechem.2020.03.083.
[21] N. Rui, F. Zhang, K. Sun, Z. Liu, W. Xu, E. Stavitski, S.D. Senanayake, J.A. Rodriguez, C.-J. Liu, Hydrogenation of CO_2 to Methanol on a $Au^{\delta+}$–In_2O_{3-x} Catalyst, ACS Catal. (2020), https://doi.org/10.1021/acscatal.0c02120.
[22] J.H. Scofield, Hartree-Slater subshell photoionization cross-sections at 1254 and 1487 eV, J. Electron Spectrosc. Relat. Phenom. 8 (1976) 129–137, https://doi.org/10.1016/0368-2048(76)80015-1.
[23] C.J. Powell, A. Jablonski, Progress in quantitative surface analysis by X-ray photoelectron spectroscopy: Current status and perspectives, J. Electron Spectrosc. Relat. Phenom. 178–179 (2010) 331–346, https://doi.org/10.1016/j.elspec.2009.05.004.
[24] C.J. Powell, A. Jablonski, NIST Electron Inelastic-Mean-Free-Path Database - Version 1.2, National Institute of Standards and Technology, Gaithersburg, MD, 2010. http://dx.doi.org/10.18434/T48C78.
[25] M. Sano, T. Adaniya, T. Fujitani, J. Nakamura, Formation Process of a Cu−Zn Surface Alloy on Cu(111) Investigated by Scanning Tunneling Microscopy, J. Phys. Chem. B 106 (2002) 7627–7633, https://doi.org/10.1021/jp012810i.
[26] T. Flores, S. Junghans, M. Wuttig, Atomic mechanisms of the formation of an ordered surface alloy: an STM investigation of MnCu(100), Surf. Sci. 371 (1997) 14–29, https://doi.org/10.1016/S0039-6028(96)00979-X.
[27] T.J. Raeker, A.E. DePristo, Alloy formation energetics and dynamics in the Ni/Cu (100) and Ni/Cu(111) systems, J. Vac. Sci. Technol. A. 10 (1992) 2396–2399, https://doi.org/10.1116/1.577972.
[28] N. Pauly, S. Tougaard, F. Yubero, LMM Auger primary excitation spectra of copper, Surf. Sci. 630 (2014) 294–299, https://doi.org/10.1016/j.susc.2014.08.029.
[29] E. Antonides, E.C. Janse, G.A. Sawatzky, Auger spectra of Cu, Zn, Ga, and Ge. I. Transition probabilities, term splittings, and effective Coulomb interaction, Phys. Rev. B 15 (1977) 1669–1679, https://doi.org/10.1103/PhysRevB.15.1669.
[30] T.K. Sham, M.L. Perlman, R.E. Watson, Electronic behavior in alloys: Gold-non-transition-metal intermetallics, Phys. Rev. B 19 (1979) 539–545, https://doi.org/10.1103/PhysRevB.19.539.
[31] P. Sadhukhan, S. Barman, T. Roy, V.K. Singh, S. Sarkar, A. Chakrabarti, S.R. Barman, Electronic structure of Au-Sn compounds grown on Au(111), Phys. Rev. B 100 (2019), https://doi.org/10.1103/PhysRevB.100.235404 235404.
[32] C. Rameshan, H. Lorenz, L. Mayr, S. Penner, D. Zemlyanov, R. Arrigo, M. Haevecker, R. Blume, A. Knop-Gericke, R. Schlögl, B. Klötzer, CO_2-selective methanol steam reforming on In-doped Pd studied by in situ X-ray photoelectron spectroscopy, J. Catal. 295 (2012) 186–194, https://doi.org/10.1016/j.jcat.2012.08.008.
[33] S. Tougaard, Energy loss in XPS: Fundamental processes and applications for quantification, non-destructive depth profiling and 3D imaging, J. Electron Spectrosc. Relat. Phenom. 178–179 (2010) 128–153, https://doi.org/10.1016/j.elspec.2009.08.005.
[34] G.K. Maira, B.R. Orton, J.C. Riviere, An XPS study of indium through the melting point, J. Phys. F Met. Phys. 17 (1987) 1999–2006, https://doi.org/10.1088/0305-4608/17/10/008.
[35] S. Aksela, High resolutionMNN auger spectra of Ag, Cd, In, Sb, Te, and I, Z. Für Phys. Hadrons Nucl. 244 (1971) 268–274, https://doi.org/10.1007/BF01395571.
[36] J.A. Rodriguez, D.W. Goodman, The Nature of the Metal-Metal Bond in Bimetallic Surfaces, Science 257 (1992) 897–903, https://doi.org/10.1126/science.257.5072.897.
[37] J.A. Rodriguez, R.A. Campbell, D.W. Goodman, Interaction of ultrathin films of copper with rhodium(100) and ruthenium(0001): an XPS study, J. Phys. Chem. 95 (1991) 2477–2483, https://doi.org/10.1021/j100159a068.
[38] E. Jeroro, M.P. Hyman, J.M. Vohs, Ensemble vs. electronic effects on the reactivity of two-dimensional Pd alloys: a comparison of CO and CH_3OH adsorption on Zn/Pd(111) and Cu/Pd(111), Phys. Chem. Chem. Phys. 11 (2009) 10457–10465, https://doi.org/10.1039/B913220A.
[39] M. Khanuja, B.R. Mehta, S.M. Shivaprasad, Geometric and electronic changes during interface alloy formation in Cu/Pd bimetal layers, Thin Solid Films 516 (2008) 5435–5439, https://doi.org/10.1016/j.tsf.2007.07.117.
[40] G. Liu, T.P. St Clair, D.W. Goodman, An XPS Study of the Interaction of Ultrathin Cu Films with Pd(111), J. Phys. Chem. B 103 (1999) 8578–8582, https://doi.org/10.1021/jp991843j.
[41] M.V. Ganduglia-Pirovano, J. Kudrnovský, M. Scheffler, Adlayer Core-Level Shifts of Random Metal Overlayers on Transition-Metal Substrates, Phys. Rev. Lett. 78 (1997) 1807–1810, https://doi.org/10.1103/PhysRevLett.78.1807.
[42] A. Regoutz, G. Kerherve, I. Villar-Garcia, C.K. Williams, D.J. Payne, The influence of oxygen on the surface interaction between CO_2 and copper studied by ambient pressure X-ray photoelectron spectroscopy, Surf. Sci. 677 (2018) 121–127, https://doi.org/10.1016/j.susc.2018.06.004.
[43] S.M. Rossnagel, H.F. Dylla, S.A. Cohen, AES study of the adsorption of O_2, CO, CO_2, and H2O on indium, J. Vac. Sci. Technol. 16 (1979) 558–561, https://doi.org/10.1116/1.569996.
[44] T. Koitaya, S. Yamamoto, Y. Shiozawa, Y. Yoshikura, M. Hasegawa, J. Tang, K. Takeuchi, K. Mukai, S. Yoshimoto, I. Matsuda, J. Yoshinobu, CO_2 Activation and Reaction on Zn-Deposited Cu Surfaces Studied by Ambient-Pressure X-ray Photoelectron Spectroscopy, ACS Catal. 9 (2019) 4539–4550, https://doi.org/10.1021/acscatal.9b00041.
[45] L. Nguyen, F.F. Tao, Y. Tang, J. Dou, X.-J. Bao, Understanding Catalyst Surfaces during Catalysis through Near Ambient Pressure X-ray Photoelectron Spectroscopy, Chem. Rev. 119 (2019) 6822–6905, https://doi.org/10.1021/acs.chemrev.8b00114.
[46] G. Greczynski, L. Hultman, Reliable determination of chemical state in x-ray photoelectron spectroscopy based on sample-work-function referencing to

adventitious carbon: Resolving the myth of apparent constant binding energy of the C 1s peak, Appl. Surf. Sci. 451 (2018) 99–103, https://doi.org/10.1016/j.apsusc.2018.04.226.
[47] X. Deng, A. Verdaguer, T. Herranz, C. Weis, H. Bluhm, M. Salmeron, Surface Chemistry of Cu in the Presence of CO_2 and H_2O, Langmuir 24 (2008) 9474–9478, https://doi.org/10.1021/la8011052.
[48] M. Favaro, H. Xiao, T. Cheng, W.A. Goddard, J. Yano, E.J. Crumlin, Subsurface oxide plays a critical role in CO_2 activation by Cu(111) surfaces to form chemisorbed CO_2, the first step in reduction of CO_2, Proc. Natl. Acad. Sci. 114 (2017) 6706–6711, https://doi.org/10.1073/pnas.1701405114.
[49] J.P. Bonnelle, J. Grimblot, A. D'huysser, Influence de la polarisation des liaisons sur les spectres esca des oxydes de cobalt, J. Electron Spectrosc. Relat. Phenom. 7 (1975) 151–162, https://doi.org/10.1016/0368-2048(75)80047-8.
[50] A. Gurlo, M. Ivanovskaya, A. Pfau, U. Weimar, W. Göpel, Sol-gel prepared In_2O_3 thin films, Thin Solid Films 307 (1997) 288–293, https://doi.org/10.1016/S0040-6090(97)00295-2.
[51] C. Janowitz, V. Scherer, M. Mohamed, A. Krapf, H. Dwelk, R. Manzke, Z. Galazka, R. Uecker, K. Irmscher, R. Fornari, M. Michling, D. Schmeißer, J.R. Weber, J.B. Varley, C.G.V. de Walle, Experimental electronic structure of In_2O_3 and Ga_2O_3, New J. Phys. 13 (2011), https://doi.org/10.1088/1367-2630/13/8/085014 085014.
[52] J.C.C. Fan, J.B. Goodenough, X-ray photoemission spectroscopy studies of Sn-doped indium-oxide films, J. Appl. Phys. 48 (1977) 3524–3531, https://doi.org/10.1063/1.324149.
[53] T. Bielz, H. Lorenz, W. Jochum, R. Kaindl, F. Klauser, B. Klötzer, S. Penner, Hydrogen on In_2O_3: Reducibility, Bonding, Defect Formation, and Reactivity, J. Phys. Chem. C 114 (2010) 9022–9029, https://doi.org/10.1021/jp1017423.
[54] H. Schoeller, J. Cho, Oxidation and reduction behavior of pure indium, J. Mater. Res. 24 (2009) 386–393, https://doi.org/10.1557/JMR.2009.0040.
[55] Y. Ren, C. Xin, Z. Hao, H. Sun, S.L. Bernasek, W. Chen, G.Q. Xu, Probing the Reaction Mechanism in CO_2 Hydrogenation on Bimetallic Ni/Cu(100) with Near-Ambient Pressure X-Ray Photoelectron Spectroscopy, ACS Appl. Mater. Interfaces (2019), https://doi.org/10.1021/acsami.9b19523.
[56] M. Roiaz, E. Monachino, C. Dri, M. Greiner, A. Knop-Gericke, R. Schlögl, G. Comelli, E. Vesselli, Reverse Water-Gas Shift or Sabatier Methanation on Ni (110)? Stable Surface Species at Near-Ambient Pressure, J. Am. Chem. Soc. 138 (2016) 4146–4154, https://doi.org/10.1021/jacs.5b13366.
[57] B. Eren, R.S. Weatherup, N. Liakakos, G.A. Somorjai, M. Salmeron, Dissociative Carbon Dioxide Adsorption and Morphological Changes on Cu(100) and Cu (111) at Ambient Pressures, J. Am. Chem. Soc. 138 (2016) 8207–8211, https://doi.org/10.1021/jacs.6b04039.
[58] E.H.P. Cordfunke, R.J.M. Konings, W. Ouweltjes, The standard enthalpy of formation of In_2O_3, J. Chem. Thermodyn. 23 (1991) 451–454, https://doi.org/10.1016/S0021-9614(05)80132-6.
[59] P.J. Linstrom, W.G. Mallard (Eds.), NIST Chemistry WebBook, NIST Standard Reference Database Number 69, National Institute of Standards and Technology, Gaithersburg MD, 20899, n.d. https://doi.org/10.18434/T4D303.
[60] A. Walsh, Surface oxygen vacancy origin of electron accumulation in indium oxide, Appl. Phys. Lett. 98 (2011), https://doi.org/10.1063/1.3604811 261910.
[61] S. Lany, A. Zakutayev, T.O. Mason, J.F. Wager, K.R. Poeppelmeier, J.D. Perkins, J.J. Berry, D.S. Ginley, A. Zunger, Surface Origin of High Conductivities in Undoped In_2O_3 Thin Films, Phys. Rev. Lett. 108 (2012), https://doi.org/10.1103/PhysRevLett.108.016802 016802.
[62] Y. Ren, K. Yuan, X. Zhou, H. Sun, K. Wu, S.L. Bernasek, W. Chen, G.Q. Xu, Catalytic Intermediates of CO_2 Hydrogenation on Cu(111) Probed by In Operando Near-Ambient Pressure Technique, Chem. – Eur. J. 24 (2018) 16097–16103, https://doi.org/10.1002/chem.201802931.
[63] J. Ye, Q. Ge, C. Liu, Effect of PdIn bimetallic particle formation on CO_2 reduction over the Pd–In/SiO_2 catalyst, Chem. Eng. Sci. 135 (2015) 193–201, https://doi.org/10.1016/j.ces.2015.04.034.
[64] J. Ye, C. Liu, D. Mei, Q. Ge, Methanol synthesis from CO_2 hydrogenation over a Pd_4/In_2O_3 model catalyst: A combined DFT and kinetic study, J. Catal. 317 (2014) 44–53, https://doi.org/10.1016/j.jcat.2014.06.002.